AIAA-2000-0416
Feedback Stabilized Laser Differential Interferometry for Supersonic Blunt Body Receptivity Experiments

T. R. Salyer, S. H. Collicott, and S. P. Schneider
School of Aeronautics and Astronautics
Purdue University
West Lafayette, IN 47907-1282

38th Aerospace Sciences Meeting & Exhibit
January 10-13, 2000 / Reno, NV

Feedback Stabilized Laser Differential Interferometry for Supersonic Blunt Body Receptivity Experiments

Terry R. Salyer *
Steven H. Collicott †
Steven P. Schneider ‡

Aerospace Sciences Laboratory
School of Aeronautics and Astronautics
Purdue University
West Lafayette, IN 47907-1282

Abstract

The laser differential interferometer is a high sensitivity, large bandwidth, nonintrusive optical diagnostic instrument ideal for low-density flow diagnostics. However, the basic system is limited to wavelength shifts less than $\lambda/10$ for the output to remain within the linear range of the device. For measurements involving larger wavelength shifts up to $\lambda/2$, active phase compensation is added to the system using a phase modulator to feedback stabilize the system. This makes possible calibrated bow shock receptivity experiments in a Mach 4 quiet-flow Ludwieg tube facility. Laser generated thermal spots are used as repeatable, controlled perturbations to the subsonic region behind the bow shock of a hemispherical nose model. Results indicate a rapidly damped oscillation within the subsonic region which is not self-sustaining. Also, the results compare well with nose-mounted Kulite results for both the hemispherical nose model and a similar forward-facing cavity model in the flush-nose configuration. This removes most of the ambiguity from earlier experiments where results are questionable due to the inherent natural ringing frequency of the Kulite pressure transducers. Additional Kulite measurements and supplemental schlieren images are also provided, and quantitative comparisons with CFD computations are now possible. The calibrated data provides benchmark results for this type of receptivity problem.

*Research Assistant, Member AIAA
†Associate Professor, Senior Member AIAA
‡Associate Professor, Senior Member AIAA

1 Introduction

The laser differential interferometer (LDI) provides measurement capabilities unmatched by other nonintrusive optical diagnostic techniques [1, 2, 3], especially for very low-density flow diagnostics. With its high sensitivity, large bandwidth, and small spatial resolution, the LDI has shown its practical use in the low density Purdue Mach 4 quiet-flow Ludwieg tube in the past [4]. Numerous applications of the technique have also been proposed and performed by others [5, 6].

Both the previous system [4] and the system used in the current experiments are capable of detecting wavelength shifts as low as $\lambda/15{,}000$ at a bandwidth of 400 kHz and a spatial resolution of 0.1 mm. But, with the previous system, the maximum phase shift allowed was limited to one tenth of the interrogation beam wavelength to remain within the calibrated linear portion of the output. A modified LDI with feedback stabilization via an active phase compensator is currently in use which removes any large unwanted phase offsets and broadens the useful range of the system to $\lambda/2$. This active phase compensation is essential for acquiring calibrated data from the bow shock receptivity experiments detailed here.

High speed blunt body receptivity is not well understood. The high speed blunt body receptivity problem involving a laser generated thermal spot impinging on the subsonic region behind the detached bow shock off a hemisphere-cylindrical model is being investigated. To obtain unambiguous data from the LDI, one of the beams must be positioned in front of the bow shock. As a result, the beam passing behind the shock encounters a higher density region

which introduces a large phase shift between the two beams (close to $\lambda/2$ in some cases). This is well outside the linear response of the LDI, so active phase compensation using an electro-optic phase modulator is required to remove the offset [2, 7]. This allows calibrated phase measurements to be made in the subsonic region at the nose of the blunt body. This quantitative set of measurements will provide a benchmark set of results for this type of blunt body receptivity experiment.

Currently, this fluids problem relating to the blunt body paradox is of interest in the field of high speed aerodynamics. CFD researchers such as Xiaolin Zhong of UCLA are computing similar flows [8, 9]. This blunt body paradox refers to the paradoxical early onset of transition and high turbulent heat transfer within the boundary layer of a blunt body in supersonic flow. Transition has been found to occur at a Reynolds number an order of magnitude lower than that predicted by instability theory on polished cold-wall heat-sink noses. Roughness is a reasonable cause for the bypass to turbulent flow, but the exact mechanism is still unknown. The paradox may also be caused by some sort of Görtler instability since streamlines coming in towards the stagnation point are sharply curved (concave) near the body. Along with roughness, the blunt body paradox may also partly contribute to the early transition on the shuttle orbiter. At high angles of attack during reentry, the shuttle is essentially a blunt body.

The subsonic region at the nose of a blunt body in supersonic flow likely holds the key to the blunt body paradox. The significance of disturbances in the freestream and their effects within the subsonic region have been considered in the past [10]. The subsonic region may act like an oscillator which feeds the boundary layer with continuous input disturbances. So, whether or not the subsonic region oscillates when perturbed is of key importance. For receptivity and transition experiments, indeed stability experiments, the spectrum of the input perturbation is important. In general, the inputs may include a wide assortment of parameters such as freestream pressure fluctuations, particles in the freestream, acoustic waves, entropy spots, surface roughness, or others. Determining what frequencies are introduced by the perturbation may be essential for understanding this type of problem.

The measurement of perturbations and small-amplitude disturbances in high speed boundary layers requires a facility which is capable of generating uniform, quiet-flow conditions in the test section [11, 12]. The Purdue quiet-flow Ludwieg tube is a low-noise facility which provides ideal flow conditions for just such measurements. Results from other typically noisy facilities produce data contaminated with the effects of large freestream pressure fluctuations [13, 14], acoustic pressure fluctuations radiating from the turbulent boundary layers along the nozzle walls [15], particles in the freestream, etc. These factors, including surface roughness on the model, can act as bypasses to turbulent flow. Flight test data is of greatest concern for comparison with ground tests [16], but due to the difficulties of flight testing, very little data exists. Without test conditions comparable to free-flight, the results obtained are ambiguous in most cases.

The repeatable, controlled perturbation in the form of a laser generated thermal spot is used to create a disturbance upstream of the model. This thermal spot then convects downstream at Mach 4 and impinges on the detached bow shock before entering the boundary layer. The LDI is used to analyze both the thermal spot in the freestream and the effect that it has on the subsonic region at the nose of the model. Schlieren imagery and simultaneous Kulite pressure measurements at the nose of the model are also used to supplement the experiments.

Apparent ringing of the subsonic region (which may be an effect of the transducer ringing) behind the bow shock has been observed in previous experiments [17]. Limited results have been obtained by both Randall [18, 19] on the hemispherical nose model and Ladoon [20] on the forward-facing cavity model with Kulite pressure transducers. The results from the LDI experiments are expected to be similar to those found from the nose-mounted pressure transducer experiments, and the earlier ambiguity with the Kulite results should be removed.

2 Facility

The Purdue quiet-flow Ludwieg tube (shown in Figure 1) is one of the few facilities capable of generating the proper flow conditions needed for the current experiments. For receptivity and transition experiments, the quiet-flow capabilities are invaluable [21], [22], [23], and[11]. The nozzle, shown in Figure 2, was designed to achieve Mach 4 flow in the 3.8 by 4.3 inch test section. The facility is considered to generate quiet flow since the rms pressure fluctuations during a run are approximately 0.05% of the mean pressure for an initial total driver pressure of 1 atm and a total temperature of 295 K. Quiet flow is maintained in the test region in large part due to the high polish (2 microinch) on the nozzle walls. This ensures that the walls of the nozzle remain laminar

over a larger area, thus reducing the noise level in the tunnel.

The test core is demarcated upstream by the start of uniform flow characteristics and downstream by the Mach lines generated by the onset of turbulence on the wind tunnel walls. The uniform flow region begins 9.33 inches along the centerline from the throat of the nozzle and is bounded by the Mach lines (Mach 4) generated from the center of the nozzle at this downstream location (see Figure 2). The quiet flow region ends approximately 4 inches beyond this starting point.

The flow in the tunnel, typically lasting approximately 3.5 seconds, is quasi-steady. The drop in pressure due to the passage of the expansion waves is approximately 1.2% of the initial total pressure behind the bow shock after quiet flow is established. Throughout the run, the stagnation pressure decreases by approximately 35% while the (absolute) stagnation temperature decreases by approximately 10%. The result is a series of 0.1 second steps totaling over 3.5 seconds.

The drop in total pressure and total temperature have been measured for the Ludwieg tube runs. From these two quantities, total density is computed. Assuming a negligible total pressure drop through the unsteady expansion process, the static flow properties are computed assuming an isentropic expansion to Mach 4. Drop in test section freestream velocity and drop in unit Reynolds number are computed as well. For the change in dynamic viscosity due to the drop in static temperature, the Sutherland law is applied. Note that the unit Reynolds number is constant to 1% during each segment (step). As the prime quantity of interest, static density is plotted for a typical run in Figure 3. Also, Table 1 contains the flow quantities measured and computed for four points (indicated in Figure 3) throughout the run.

3 Instrumentation

3.1 Test Model

The stainless steel model has a one inch diameter hemispherical nose and a cylindrical frustum. In the tip of the model is inserted a small Kulite pressure transducer (model XCQ-062-25A) to measure the total pressure fluctuations behind the bow shock. The absolute pressure transducer has a rated operational pressure of 25 psia and has been custom manufactured with no screen and a flush RTV surface. The diameter of the Kulite is 0.064 inches and the mounting hole is 0.067 inches in diameter. Since the transducer has a flat face and is flush mounted, the tip of the model is flat over a small area. Also note that the gap between the transducer and the edge of the hole is filled, so the flat region at the tip is actually 0.067 inches in diameter. This accounts for approximately 0.5% of the frontal area of the model. The manufacturer claims that the transducer has a natural frequency of 500 kHz, but the actual ringing frequency, as reported in reference [18], has been measured to be much lower (approximately 200 kHz).

Recall that the start of uniform flow is located at 9.33 inches downstream of the nozzle throat. Since the quiet-flow region is small, the models are moved forward as much as possible. In the current experiment, the model tip is located at 10.69 inches downstream of the nozzle throat along the centerline. This means that, with a one inch diameter nose, the shoulders of the model protrude slightly outside the uniform flow region. But, the subsonic region of the model is well within the quiet, uniform flow.

The bow shock standoff distance has been measured (using a schlieren image, see Figure 16) to be approximately 20% of the 0.5 inch radius of the blunt body (0.1 inches). Another measured value, according to Liepmann and Roshko [24], for a 0.5 inch radius sphere in Mach 4 flow is 0.08 inches. The sonic lines at the model nose are located at an approximate 45° angle from the center of the hemisphere [25]. Thus, about half the frontal area of the hemisphere is included in the subsonic region. An illustration of the blunt body in the test flow configuration can be seen in Figure 4 where the extent of the subsonic region has been exaggerated.

Results using the hemispherical nose model are compared with results from a forward-facing cavity model. This model generates definite ringing frequencies which can be adjusted by modifying the length of the cavity. In the flush-nose configuration, the results should be similar to those obtained with the hemispherical nose model. Results have already been obtained from the cavity base mounted Kulite (see reference [20]), so the LDI will likely indicate similar ringing behavior. The forward-facing cavity model has a 0.375 inch nose radius with a 0.375 inch diameter cavity in the front (or a 0.375 inch flat front surface in the flush-nose configuration). About one inch back, the model flares from a 0.750 inch diameter to a 1.000 inch diameter over approximately one inch.

3.2 Controlled Perturbation

To perform receptivity experiments, some form of controlled, repeatable perturbation is needed [26, 27, 28, 29, 30]. It is preferable that both the amplitude and frequency of the disturbance be controlled, although in practice this is often difficult to do. For the experiments discussed here, an external perturbation in the form of a laser generated thermal spot is used. The amplitude is adjusted with the laser power, and the thermal spot size and associated perturbation frequency can be slightly adjusted with initial spot positioning as well as laser power.

A Spectra Physics model GCR 190 Nd:YAG laser is used as the light source for generating the thermal 'hot spots'. By focusing the high energy beam into the test section upstream of the model, a small thermal spot is created. Initially the process creates a small ball of plasma (and associated initial shock wave) by photo-ionizing the air in the test section. The plasma then quickly reassociates and leaves a local thermal spot surrounded by an expanding weak shock formed during generation of the spot. This thermal spot then convects downstream and becomes the controlled perturbation.

The laser is injection seeded for narrow bandwidth and consistent shot-to-shot energy output, and is frequency doubled to 532 nm. The monochromatic beam is pulsed at 10 Hz with a pulse duration of approximately 7 ns. The maximum energy output of the laser is 260 mJ per pulse, but perturbation energies used for the experiments are around 230 mJ per pulse. The optics system used to direct and focus the beam is shown in Figure 5. Note that the beam must be oriented at an angle of approximately 5 degrees (to the test section window perpendicular) to avoid damage caused by back reflections from the second test section window.

Details of the thermal spot generation system and a description of the changing size and shape of the spot can be found in references [31], [32], and [33]. More recent detailed studies of the thermal spot have been performed with the LDI. Thermal spot amplitudes, spatial characteristics, and repeatability aspects are presented in [4]. During the run, the spot grows as it travels downstream. When it hits the bow shock and hemispherical model approximately 45 μs after the thermal spot is created, the LDI indicates an approximately 5 mm diameter thermal spot with corresponding 10 mm weak shock radius. The weak shock is undetectable from hot wire studies, although the width of the spot itself based on half the maximum amplitude has been also measured as approximately 5 mm [34].

3.3 Laser Differential Interferometer

The laser differential interferometer (LDI) is a nonintrusive instrument with both high sensitivity and large bandwidth. Currently, the system is capable of measuring wavelength shifts (density changes) as low as $\lambda/15{,}000$ with a flat (0.5 dB maximum loss) bandwidth of 400 kHz. Modifications to receiver electronics will allow much higher bandwidths. The system also possesses a high spatial resolution with a current probe size (beam diameter) of 0.1 mm. This property is also easily changed with modification of the system optics. The system works by detecting the rapid phase shift between two narrowly spaced, tightly focused beams sent through the test volume. Calibration of the system is also simple so that quantitative phase shifts are easily determined.

The qualities mentioned above give the LDI a distinct advantage over other interferometric, schlieren, and shadowgraph techniques. It is also relatively inexpensive, and reduction of data to optical path difference is possible. Note that the LDI is only capable of examining one integrated line (or a series of integration lines) in the flowfield through time. Although other types of interferometers visualize an entire region of a flowfield, they lack the extreme sensitivity and high temporal resolution of the LDI. Like all interferometers and phase sensitive optical systems, the LDI must deal with a finite integration length of beams through the test section.

The basic LDI system sends two closely spaced, narrow beams through the test section which are then interfered on a photodetector, as shown in Figure 6. From one low power (greater than 1.0 mW), intensity stabilized He-Ne laser, the two beams are formed and recombined through a series of Wollaston prisms, quarter-wave plates, achromatic lenses, and a polarizer (if the laser is not already polarized). An additional Wollaston prism splits the recombined beams into two pairs of beams with complementary interferences. The relative change in light intensity due to the interference in the beam pairs is detected with two high-speed photodiodes. With no phase shift between the two beams in the test section, the intensity of each interfering beam pair is the same while the interferometer is adjusted to the infinite fringe spacing. The phase relation between the interfering beams of each pair corresponds to the linear part of an interference slope between a light and dark band (see Figure 7). Small optical path changes by a phase object in the test section lead to light level changes on the photodiodes, and hence electrical signal changes in the photodiode circuitry. This

relation is given by

$$\frac{\Delta E}{E_\circ} = \frac{\Delta U}{U_\circ} = 2\pi \frac{\delta \Phi}{\lambda} \Longrightarrow \delta \Phi = \frac{\lambda}{2\pi} \frac{\Delta E}{E_\circ} \qquad (1)$$

where U corresponds to light intensity, E is the voltage at the photodiode circuit, $\delta\Phi$ is the difference in optical path length, and λ is the wavelength of the laser light (632.8 nm). $E_\circ$ is the voltage calibration value which must be determined prior to the experiment. By differencing the electrical signals (recall that the signals are complementary) from the two photodiodes across one load resistor, a signal which is doubled in amplitude is created while simultaneously suppressing noise in the signal due to laser light fluctuations. The simple circuit which performs this task is shown in Figure 8. Note that the object in the test section must be imaged onto the photodiodes to avoid any schlieren effects. Spatial density or index of refraction gradients cause light rays to bend and also alter in phase. Interferometers function on the second phenomenon, and so the imaging lens is used to negate the first effect. For more details on the LDI system, see reference [2].

Accurate qualitative results require that the system frequency response be flat up to the frequency of the input disturbance. The maximum flat (0.5 dB maximum loss) frequency response (400 kHz) and minimum detectable phase shift (0.042 nm for the 632.8 nm interrogation beam) mentioned earlier are results of earlier tests detailed in reference [4]. These results were obtained using a 5 kΩ load resistor, which is the same for the current experiments. The signal-to-noise ratio, if too small, may be increased by increasing the size of the load resistor, albeit decreasing the bandwidth of the system. Fortunately, increasing the size of the load resistor does not noticeably increase the baseline noise in the photodiode circuit (around 1.8 mV peak-to-peak). The maximum signal-to-noise ratio observed in the freestream thermal spot studies is approximately 75, which corresponds to a phase shift of approximately $\lambda/180$ (well within the linear region of approximately $\lambda/10$).

With only one beam behind the shock for the bow shock experiments, the phase shift is much larger and is well outside the acceptable linear range of the LDI response. The results are no longer quantitative since the linear calibration is no longer valid. To maintain the original quantitative benefits of the system, the large phase offset between the two LDI beams must be removed with an added phase compensating device. Only the phase offset in the beams due to the bow shock is removed while the higher frequency signals from the thermal spot impingement register normally.

An electro-optic phase modulator is needed. These modulators are transverse, low voltage, electro-optic light modulators which work on the Pockels effect. The systems consist of two main parts, the modulator itself and its high voltage driver. Here, a Quantum Technology, Inc. model 28P ADP 2.5 mm aperture phase modulator is used with a model HVA-100K high voltage driver. This system is capable of half-wave phase modulating a 633 nm beam up to 250 kHz, well beyond the active phase compensation frequency needed.

With or without the phase modulator, the basic LDI system is the same. The compensator (feedback stabilization) is simply an add-on component to the basic system. The phase modulator is inserted into the system after the second Wollaston prism and before the last quarter-wave plate (see basic layout in Figure 6). Here, the beams are coincident but are not yet capable of interfering since their polarizations are still orthogonal. The phase modulator is oriented such that its optical axis is aligned with the polarization of one of the beams. When activated, the modulator can then alter the phase of this beam.

Since the modulator needs to compensate for the large, lower frequency phase shift caused by the bow shock, the output signal from the photodiode circuit is low-pass filtered (5 Hz or 50 Hz) and fed back to the high voltage driver which then amplifies the signal and controls the phase modulator to remove the offset (see Figure 8). The simple feedback circuit stabilizes the LDI about the center of the linear region of the interference slope, and always returns the system to equilibrium. The higher frequency signal from the thermal spot impinging on the bow shock is picked off at the photodiode receiver and does not pass through the low-pass filter to the phase modulator. With this active feedback stabilization system, the quantitative properties of the LDI remain intact. See references [2] and [7] for additional details.

3.4 Schlieren System

The schlieren system used for these experiments is a standard Z-formation mirrored type and is set up on the same vibrationally isolated breadboard system as the laser differential interferometer and thermal spot generation system (see Figure 9 for details). The system allows a full window field of view and various higher magnifications to examine the thermal spots and model nose region.

The system uses an EG&G 1100 series high stability short arc Xenon flashlamp as a pulsed light source, and images are acquired with an NEC model TI-324A CCD camera and Poynting Products VFD4

single-frame video capture system which can be triggered at some pre-set time after an event, such as the laser firing. The light source is bright enough and the pulse duration is short enough (1 μs) to acquire decent images of the Mach 4 flow features. The firing of the tunnel, light source, and camera are all triggered using a Quantum Composers model 9310 pulse generator. The 10 Hz laser Q-switch synchronization signal is used as an input trigger to the pulse generator, and marks the generation of the thermal spot. The pulse generator fires the tunnel on command (synchronized with the laser pulse with a few microseconds of scatter) and after 10 laser pulses (1.0 s delay) the pulse generator triggers the light source and camera with some pre-set delay after the laser pulse. In this manner, the laser spot and its effect on the bow shock can be captured at any time after the thermal spot generation by varying the delay on the pulse generator.

Since the density inside the test section is very low (see Figure 3), great care must be taken to ensure that spatial density gradients outside the test section are reduced as much as possible. Otherwise, the low density objects of interest inside the test section may be completely obscured by the much larger, spurious density gradients outside the test section. Improvements may be possible with the use of a multiple-source schlieren system [35].

4 Receptivity Experiments

For the blunt body receptivity experiments in this paper, characterization of the thermal spot is necessary. Reference [4] gives spot dimensions, growth rates, and phase shift profiles. Both the LDI and the thermal spot generation technique are very repeatable (within a few percent). Also, the current generation of receiver electronics is sufficient for the thermal spot and bow shock oscillation studies (see reference [4]).

All the experiments are performed using lowered driver tube total pressures of approximately 9.8 psia (2/3 atm) and driver tube total temperatures of approximately 77 degrees F. These conditions prevent turbulent spots from forming on the test section windows and also help to ensure quiet flow conditions in the test section. The approximate initial flow parameters for each run are as follows: a freestream velocity of 675 m/s, a unit Reynolds number of 31,000/cm, and a freestream static density of 0.022 kg/m^3. Over the course of the run, the velocity decreases by approximately 7%, the unit Reynolds number decreases by approximately 29%, and the freestream static density decreases by approximately 36% (see Table 1).

In all runs, the thermal spot is generated approximately 20 mm upstream of the LDI beams (see Figure 4). Positioning accuracy of the thermal spot in the freestream direction is approximately $\pm$1 mm. In the vertical cross-stream direction, the positioning accuracy is approximately $\pm$0.1 mm. And, in the horizontal cross-stream direction (in the direction of the LDI beams), the positioning accuracy is approximately $\pm$2 mm. The beams of the LDI are oriented horizontally for all tests so that the freestream direction is in the plane of the beams. Also, the beam spacing is approximately 7.4 mm and the focused spot size in the center of the test section is approximately 0.1 mm. The signal acquired is sampled at 5 MHz, with both scopes and the firing of the tunnel being triggered off the pulse generator which is synchronized with the laser pulses.

The diagnostic systems (LDI, schlieren, and thermal spot generation optics) are mounted on the vibrationally isolated optics table which is not fixed relative to the wind tunnel. Because the model and the test section actually move axially (approximately 1 mm) when the tube is pumped down to run conditions (the tunnel compresses), the thermal spot and LDI are aligned after the tunnel is ready for each run. From schlieren images before, during, and after the runs, it is noted that the model does not move significantly during the run, so the alignment before the run is maintained. Except for the freestream thermal spot studies where both LDI beams are positioned in the freestream, the beams are positioned such that the upstream beam is always in the freestream ahead of the bow shock, and the downstream beam is behind the bow shock at designated location x from the nose. The beams are positioned with a Velmex traverse (0.001 inch increments) and the estimated positioning error is $\pm$0.05 mm. The vertical positioning error is approximately $\pm$0.1 mm.

4.1 LDI Results

The initial bow shock receptivity experiments reported in reference [4] were conducted with a 1.1 mm beam spacing. With both beams sent through the subsonic nose region of the blunt body, oscillations were detected from the impingement of the thermal spot. However, due to ambiguity from the integration of the two closely spaced beams, difficulty existed in determining any characteristic ringing frequencies of the subsonic region. Now, with the upstream beam outside the bow shock acting as a reference beam, most of the ambiguity from the beam

integration issue is removed.

The signal obtained from the thermal spot impingement on the bow shock is the sum of the phase shift due to the thermal spot and the phase shift due to the ringing or disturbance of the subsonic region caused by the thermal spot. If the signal from thermal spot behind the bow shock were known, the two disturbances could be effectively separated by subtracting it from the combined LDI signal. But, the thermal spot deforms as it passes through the bow shock in some unknown manner (not visible with the schlieren studies), so the freestream thermal spot signal cannot simply be subtracted from the bow shock signal.

Figure 10 illustrates how the system actively compensates for the large phase shift in the system. The voltage across the feedback capacitor is fed back through the high voltage amplifier to the phase modulator. Since the LDI automatically remains tuned to the linear portion of the interference slope, the signal remains calibrated, and the low frequency drift in the system is removed. Before each run, the LDI is detuned by approximately $\lambda/4$ to ensure that the LDI remains in a stable region of the interference slope when the phase is shifted by the bow shock. This initially charges the capacitor negatively, and when the phase compensator is activated and the gain is increased, the LDI shifts back to the center of the linear portion of the interference slope (see Figure 7). From the signals in Figure 10, it is apparent that the maximum phase offset (for $x = 0.1$ mm) is around $\lambda/4$ since the capacitor voltage required to stabilize the system moves close to zero at the beginning of the run. As the run progresses, note the gradual decrease in the feedback voltage. This is expected since the density across the bow shock decreases throughout the run.

The upper limit of the modulation frequency is set by the low-pass filtering of the photodiode receiver output. Figure 10 indicates results from two different feedback capacitors, one an order of magnitude larger than the other. Subsequently, the response time of the system is altered by one order of magnitude as well. With the 1.0 μF capacitor, the system responds in approximately 0.2 seconds (5 Hz), and with the 0.1 μF capacitor, the system responds in approximately 0.02 seconds (50 Hz). For the run indicated with both beams in the freestream, the feedback voltage remains approximately constant, with small changes resulting from low frequency LDI drift due to thermal currents in the room or fluctuating He-Ne laser power.

Figure 11 shows the response of the LDI to the passage of the thermal spot in the freestream. The effects of both the shock and the thermal spot are clearly visible. The two small peaks (the first indicated with an A in the figure) at the beginning and end of the signal are from the weak shock expanding around the thermal spot. The two large peaks (the first indicated with a B in the figure) in the center portion are from the passage of the thermal spot. Two peaks are acquired since the spot passes once through each beam. The peaks are opposite in sign since the phase is differenced between the two beams. Note that the effect of the leading edge of the shock passing through the downstream beam is visible in the center portion of the signal as well as the effect of the trailing edge of the shock passing through the upstream beam. Three different signals are indicated in the figure, two from different size feedback capacitors and one from the uncompensated system. In the freestream, active phase compensation is not necessary since the only phase shift in the beams occurs from the small influence of the thermal spot. But, using the active phase compensation reduces the low frequency LDI drift. Since all three signals are approximately the same, it can be deduced that the low-pass filtering with the two indicated capacitors is low enough to not affect the bandwidth of the output across the load resistor.

The response from the thermal spot impinging on the bow shock with the downstream LDI beam positioned 0.1 mm from the nose of the model is indicated in Figure 12. This signal contains the influence on the LDI beams from both the thermal spot and the disturbance it causes within the subsonic region. Note that the effect from the thermal spot passing through the beam in front of the bow shock is the same as that in the freestream (indicated by the same peaks A and B that were also shown in Figure 11). Once the shock and thermal spot enter the subsonic region though, the signal clearly indicates some other response. The vertical dashed line indicates the time the perturbation enters the subsonic region. Three different signals are shown, two with the same capacitor for repeatability measurements, and one with a different capacitor to see if the bandwidth or system response changes at a different feedback frequency. The two signals with the 1.0 μF feedback capacitor are virtually the same, and were performed without realigning the LDI or the thermal spot generating optics. The signal from the 0.1 μF feedback capacitor is also nearly the same, except for the discrepancy near the end of the response. This run was performed after other runs with different LDI and thermal spot positioning, so some error in repositioning may be the cause of the small discrepancy.

A survey of LDI signals throughout the bow shock region is shown in Figure 13. The LDI was positioned in 0.5 mm increments, starting 0.1 mm from the nose of the model. This gives five survey locations within the subsonic region, with one location just outside the bow shock (at $x = 2.6$ mm). The response to the thermal spot in the freestream is also shown. Some clear initial ringing, superimposed on a lower frequency oscillation, is present. Note how the signal changes monotonically throughout the subsonic region. The strongest response occurs just behind the bow shock, but the initial ringing frequency seems more prominent near the nose. The initial ringing frequency corresponds to roughly 5 μs per cycle, which is approximately 200 kHz. Considering the perturbation frequency of the spot, where a 5 mm thermal spot traveling at 660 m/sec gives 132 kHz, the frequencies are similar. Note that both oscillations seem to damp out quickly. The whole oscillation appears to decay in under 80 μs. The impingement of the thermal spot causes a definite ringing, but the oscillation is not self-sustaining at these conditions. Note that all of the data segments are from 1.5 seconds into each run.

Receptivity of the thermal spot into the subsonic region is analyzed with results indicated in Figure 14. The perturbation amplitude (denoted by peak B in Figures 11 and 12) is determined for each data segment throughout the run, and the induced response amplitude (judged by the maximum positive amplitude in the signal) is determined as well. The induced response to perturbation amplitude ratios are computed, and plotted throughout the run as a function of unit Reynolds number. Note that this also corresponds to thermal spot (perturbation) amplitude, which is roughly linear throughout the run. Data sets are indicated for each of the LDI positions within the subsonic region. The amplitude ratios are much higher farther from the nose (with slightly more scatter), and the response appears linear for lower unit Reynolds number (smaller perturbation amplitudes). The drop in amplitude ratio at higher unit Reynolds numbers is probably from a small nonlinearity in perturbation amplitudes at higher pressures, but it could indicate a break to other nonlinear effects as well.

4.2 Pressure Transducer Results

Additional pressure measurements have been taken with the Kulite pressure transducer at the nose of the hemisphere-cylindrical model with the thermal spot impinging. The resulting ringing of the subsonic region, similar to the results obtained in reference [18], are compared with the simultaneous LDI data and shown in Figure 13. Each pressure transducer data segment comes from the exact thermal spot detected by the LDI and shown in the adjacent column. The bold lines indicate results which have been low-pass filtered at 100 kHz, whereas the original unfiltered (except for the AC coupling from the scope) results are indicated by the lighter lines. Although all the Kulite signals are similar, ideally they should be the exact same since the thermal spot positioning should be the same. The differences are due to thermal spot alignment difficulties in the cross-stream direction. The LDI is not as sensitive to slight cross-stream misalignments since the beams pass through the test section in the direction of the misalignment, and are integrating through a larger portion of the subsonic region.

The independent measurements from the LDI presented in Figure 13 help substantiate the evidence proposed by previous Kulite pressure transducer experiments. The results indicate a ringing of the subsonic region similar to that found by other Purdue researchers on the same and similar models. Figure 15 shows Kulite pressure transducer results (from both the same hemispherical nose model used in this research and a blunt-nose forward-facing cavity model) along with LDI results nearest to the nose. The hemispherical nose results from Randall (shown as the third trace in Figure 15 [17]), filtered at 100 kHz to remove the Kulite ringing frequency, are remarkably similar to those obtained with the LDI. The duration of the oscillation is also approximately 100 μs and indicates the same initial higher frequency ringing on top of the slightly lower frequency oscillation. The results for the forward-facing cavity model (flush-nose case) obtained by Ladoon et. al. in their cavity flow experiments [20] are also similar in shape and contain the same distinguishing features. The higher frequency ringing on top of the slightly lower frequency oscillation is again present, although the amplitude and duration of the signal is different. This is to be expected though since the model nose geometry is slightly different. Still, this similar blunt model exhibits the same sort of response. Differences between the new Kulite results from the current research (the second trace in Figure 15) and the results from earlier studies by Randall (the third trace in Figure 15) are likely the result of thermal spot misalignment and possible aging of (or damage to) the pressure transducer, which is the same as that used in the earlier studies.

4.3 Schlieren Results

A schlieren system has been used to better visualize the response of the thermal spot as it is processed through the bow shock of the hemispherical nose model. Although the schlieren is only qualitative, it supplements the LDI, which only provides point-wise (or integrated line) data and is difficult to traverse vertically through the area of interest. The schlieren is not sensitive enough to visualize the spots in the freestream, but the effects on the bow shock are visible as the thermal spot impinges. This schlieren drawback only helps to aggrandize the capabilities of the LDI.

Figure 16 shows the bow shock in front of the hemispherical nose at Mach 4. There are no thermal spots impinging on the bow shock in this case. The image is to scale, so the bow shock standoff distance (0.1 inches) can be accurately measured. Note that the knife edge is oriented vertically. Figure 17 shows two images (zoomed in on the nose region) taken from a movie generated with the images from 12 different runs. Each run uses a different sequential time delay from the laser spot generation. The left image at $t = 32$ μs is just before the thermal spot hits the bow shock. The right image at $t = 38$ μs is near the peak of the disturbance from thermal spot impinging on the bow shock. Note the rounded protrusion from the bow shock. This disturbance grows and subsides in approximately 22 μs. The maximum shock standoff is approximately 0.12 inches (protrusion height in the x direction of 0.02 inches) and the maximum width in the y direction of the perturbed region is approximately 0.13 inches. Oscillations along the bow shock (if they exist as expected) are not currently visible.

Figure 18 shows four images taken from another generated movie, with time delays from the thermal spot generation shown. Again, each image is taken independently with a different time delayed trigger of the light source and camera from the pulse generator synchronized with the laser pulse. In these images there is no flow in the tunnel, and the thermal spots are generated at atmospheric conditions at the threshold laser power for generating thermal spots. These images depict how the laser-generated perturbation evolves through time. The perturbation consists of two parts, the expanding weak shock and the core thermal hot spot. While the shock continuously expands and gets weaker (approaching Mach 1), the growth of the thermal spot slows rapidly and the spot essentially remains the same size. Note the small inherent delay in the whole system since the $t = 0$ μs (which is the time delay set on the pulse generator) image already shows some thermal spot evolution. The scatter of the system is on the order of a few microseconds. Also note the reflected shock from the nose of the model in the last image.

5 CFD Comparison

To compare with experimental bow shock results from both the LDI and flush-mounted Kulite, an analysis of the CFD results of the same flow conditions, excitation disturbance, and model geometry is to be performed. With the flow field computed, comparisons to the experimental results can be made by integrating along lines through the data corresponding to the LDI beam paths.

In their study of the region behind the bow shock of a hemisphere-cylinder in response to an entropy wave disturbance, Zhong and Joubert found that "the induced oscillation of the bow shock creates strong vorticity disturbances which convect near the surface along streamlines" [8]. Results more representative of the current receptivity experiments have been requested in a collaboration with the above authors.

6 Conclusions

With its high sensitivity, large bandwidth, and small spatial resolution, the nonintrusive feedback stabilized laser differential interferometer has again shown its practicality in the low-density environment of the Purdue Mach 4 quiet-flow Ludwieg tube.

Using the thermal spot generated with the laser perturber as a controlled, repeatable disturbance to the subsonic region of a hemisphere-cylindrical model, successful receptivity experiments have been carried out. Results indicate a rapidly damped oscillation within the subsonic region which is not self-sustaining in the quiet-flow conditions of the Ludwieg tube. The signal changes monotonically throughout the subsonic region, with a larger response near the edge of the shock and more ringing near the nose of the model. Over the Reynolds number range of the tunnel, the induced response to perturbation amplitude ratios indicate a fairly linear response to the perturbation as the spot amplitude increases.

The results compare well with nose-mounted Kulite results for both the hemispherical nose model and the forward-facing cavity model in the flush-nose configuration. The frequency content, shape, and duration of the LDI signal are similar to that of the pressure transducer signals. This removes most of the ambiguity from the earlier Kulite exper-

iments where results are questionable due to the inherent natural ringing frequency of the Kulite pressure transducer.

The feedback stabilized version of the LDI allows calibrated measurements to be taken even with large, continuously changing phase offsets. This also helps to stabilize the system with respect to low frequency oscillations from thermal currents and laser power fluctuations. Quantitative comparisons can now be made with CFD computations of the same flowfield and perturbation. Also, this final data provides benchmark results for this type of receptivity problem.

Additional pressure transducer results support earlier Kulite results and also indicate how well the thermal spot is aligned with the model during each run. Also, schlieren images of the bow shock region indicate a small hemispherical protrusion at the nose of the bow shock when the thermal spot impinges and gives some indication of the receptivity of the thermal spot into the subsonic region.

Acknowledgements

Both Günter Smeets and Freddy George of the French-German Research Institute (ISL), Saint-Louis, France for their helpful suggestions, dissemination of LDI knowledge, and time spent with the author demonstrating setup of the LDI system. The Air Force Office of Scientific Research for providing funding (contract number F49620-97-1-0037). Dale Ladoon for use of the sketches of the Ludwieg tube and the Mach 4 quiet-flow nozzle.

References

[1] G. Smeets. Interferometry. Technical Report CO 214/90, French-German Research Institute (ISL), Saint-Louis, France, 1990.

[2] G. Smeets. Flow diagnostics by laser interferometry. *IEEE Transactions on Aerospace and Electronic Systems*, AES–13(2), March 1977.

[3] G. Smeets. Laser-differential interferometer applications in gas dynamics. Translation of Technical Report CO 28/73, French-German Research Institute (ISL), Saint-Louis, France, 1973. DTIC AD–A307459.

[4] Terry R. Salyer, Laura A. Randall, Steven H. Collicott, and Steven P. Schneider. Use of laser differential interferometry to study receptivity on a hemispherical nose at Mach 4. In *AIAA 36^{th} Aerospace Sciences Meeting and Exhibit*, Reno, Nevada, January 1998. AIAA 98–0238.

[5] M. Azzazy, D. Modarress, and J. Trolinger. Feasibility study of optical boundary layer transition detection. Contractor Report NASA-CP-178109, NASA, 1986.

[6] J. E. O'Hare. A nonperturbing boundary-layer transition detector. Technical Report AEDC-TR-85-62, Arnold Engineering Development Center, November 1985.

[7] G. Smeets and A. George. Laser-interferometer with phase compensation. Translation of Technical Report R 136/75, French-German Research Institute (ISL), Saint-Louis, France, 1975. DTIC AD–A307458.

[8] X. Zhong and X. Joubert. Bow-shock/disturbance interaction for hypersonic flow over a cylinder. In *20^{th} International Symposium on Shock Waves*, Pasadena, California, July 1995.

[9] Chien-Erh Chiu and Xiaolin Zhong. Numerical simulation of transient hypersonic flow using the essentially nonoscillatory schemes. *AIAA Journal*, 34(4):655–661, April 1996.

[10] M. V. Morkovin. Note on the assessment of flow disturbances at a blunt body traveling at supersonic speeds owing to flow disturbances in free stream. *Journal of Applied Mechanics*, pages 223–229, June 1960.

[11] S. P. Schneider, C. E. Haven, J. B. McGuire, S. H. Collicott, D. Ladoon, and L. A. Randall. High speed laminar-turbulent transition research in the Purdue quiet-flow Ludwieg tube. In *AIAA 18^{th} Aerospace Ground Testing Conference*, Colorado Springs, Colorado, June 1994. AIAA 94–2504.

[12] G. B. Schubauer and H. K. Skramstad. Laminar boundary-layer oscillations and stability of laminar flow. *Journal of the Aeronautical Sciences*, 14(2):69–78, February 1947.

[13] Dennis M. Bushnell. Notes on initial disturbance fields for the transition problem. Technical report, NASA Langley Research Center, Hampton, Virginia, March 1989. NASP Technical Memorandum 1051.

[14] Eli Reshotko. A program for transition research. In *AIAA 12^{th} Aerospace Sciences Meeting*, chapter Recent Developments in Boundary-Layer Transition Research. NASA transition

study group, Washington, D.C., January–February 1974. AIAA Paper 74–130.

[15] Leslie M. Mack. Linear stability theory and the problem of supersonic boundary-layer transition. *AIAA Journal*, 13(3):278–289, March 1975.

[16] Kenneth F. Stetson. Boundary-layer transition on blunt bodies with highly cooled boundary layers. *Journal of the Aero / Space Sciences*, 27(2):81–91, February 1960.

[17] Steven P. Schneider, Steven H. Collicott, J. D. Schmisseur, Dale W. Ladoon, Laura A. Randall, Scott E. Munro, and Terry R. Salyer. Laminar-turbulent transition research in the Purdue Mach-4 quiet-flow Ludwieg tube. In *19^{th} AIAA Advanced Measurement and Ground Testing Technology Conference*, New Orleans, LA, June 1996. AIAA 96–2191.

[18] Laura A. Randall. Receptivity experiments on a hemispherical nose at Mach 4. Master's thesis, School of Aeronautics and Astronautics, Purdue University, West Lafayette, IN, May 1996.

[19] Mario A. Rotea, Laura A. Randall, Ge Song, and Steven P. Schneider. Model identification of a Kulite pressure transducer. In *19^{th} AIAA Advanced Measurement and Ground Testing Technology Conference*, New Orleans, LA, June 1996. AIAA 96–2278.

[20] Dale W. Ladoon, Steven P. Schneider, and John D. Schmisseur. Physics of resonance in a supersonic forward-facing cavity. *Journal of Spacecraft and Rockets*, 35(5):626–632, September–October 1998.

[21] Steven P. Schneider and Christine E. Haven. Mean flow and noise measurements in the Purdue quiet-flow Ludwieg tube. In *AIAA 32^{nd} Aerospace Sciences Meeting and Exhibit*, Reno, Nevada, January 1994. AIAA 94–0546.

[22] Steven P. Schneider. A quiet-flow Ludwieg tube for experimental study of high speed boundary layer transition. In *AIAA 17^{th} Aerospace Ground Testing Conference*, Nashville, Tennessee, July 1992. AIAA 92–3885.

[23] Steven P. Schneider and Christine E. Haven. Quiet-flow Ludweig tube for high-speed transition research. *AIAA Journal*, 33(4):688–693, April 1995.

[24] H. W. Liepmann and A. Roshko. *Elements of Gasdynamics*. Galcit Aeronautical Series. John Wiley & Sons, Inc., New York, 1957.

[25] John D. Anderson. *Hypersonic and High Temperature Gas Dynamics*. McGraw-Hill Publishing Company, 1989.

[26] James M. Kendall. Experimental methods and results on supersonic boundary-layer stability and receptivity. Oxford University Press, edited by T. Corke et. al., 1993. To appear in the proceedings of an ICASE short course on stability and transition.

[27] W. S. Saric, H. S. Reed, and E. J. Kerschen. Leading edge receptivity to sound: Experiments, DNS, and theory. In *25^{th} AIAA Fluid Dynamics Conference*, Colorado Springs, Colorado, June 1994. AIAA 94–2222.

[28] W. Saric, J. Hoos, and R. Radezisky. Boundary-layer receptivity of sound with roughness. In *Boundary Layer Stability and Transition to Turbulence ASME*, pages 17–22, 1991. FED-Vol. 114.

[29] Eli Reshotko. Environment and receptivity. In *North Atlantic Treaty Organization Advisory Group for Aerospace Research and Development, Special Course on Stability and Transition of Laminar Flow*, pages 4–1–4–11. Specialised Printing Services Limited, Loughton, Essex, June 1984. AGARD–R–709.

[30] R. G. Batt and H. H. Legner. A review of roughness-induced nosetip transition. *AIAA Journal*, 21(1):7–22, January 1983.

[31] Joseph B. McGuire. Fluid dynamic perturbations using laser induced breakdown. Master's thesis, School of Aeronautics and Astronautics, Purdue University, West Lafayette, IN, August 1994.

[32] Steven P. Schneider, Joseph B. McGuire, Steven H. Collicott, and Terry R. Salyer. Laser-generation of controlled localized perturbations for boundary-layer transition research. In *The 16^{th} International Congress on Instrumentation in Aerospace Simulation Facilities*, Wright Lab., Wright Patterson Air Force Base, Ohio, 1995. Proceedings of an IEEE Conference at Wright Lab.

[33] John D. Schmisseur, Steven P. Schneider, Terry R. Salyer, and Steven H. Collicott. A

repeatable laser-generated localized perturbation for application to fluid mechanics. In *Eighth International Symposium on Applications of Laser Techniques to Fluid Mechanics*, Lisbon, Portugal, July 1996.

[34] John D. Schmisseur. *Receptivity of the boundary layer on a Mach-4 elliptic cone to laser-generated localized freestream perturbations.* PhD thesis, School of Aeronautics and Astronautics, Purdue University, West Lafayette, IN, December 1997.

[35] T. R. Salyer. Quantitative noise reduction measurements of a multiple-source schlieren system. Master's thesis, School of Aeronautics and Astronautics, Purdue University, West Lafayette, IN, May 1994.

Quantity	0.3 sec flow time	1.3 sec flow time	2.3 sec flow time	3.3 sec flow time
1	9.4072E+00	8.1303E+00	7.0833E+00	6.2318E+00
2	6.4862E+04	5.6058E+04	4.8840E+04	4.2968E+04
3	4.2719E+02	3.6921E+02	3.2166E+02	2.8299E+02
4	7.1232E+01	5.2799E+01	3.5383E+01	1.9718E+01
5	2.9495E+02	2.8471E+02	2.7503E+02	2.6633E+02
6	7.0225E+01	6.7787E+01	6.5483E+01	6.3411E+01
7	7.6678E-01	6.8654E-01	6.1918E-01	5.6254E-01
8	2.1210E-02	1.8991E-02	1.7127E-02	1.5561E-02
9	6.7168E+02	6.5991E+02	6.4860E+02	6.3826E+02
10	2.9992E+04	2.7444E+04	2.5291E+04	2.3449E+04

Quantity	Description
1	total pressure in psia
2	total pressure in N/m^2
3	freestream static pressure in N/m^2
4	total temperature in degrees F
5	total temperature in K
6	freestream static temperature in K
7	total density in kg/m^3
8	freestream static density in kg/m^3
9	freestream velocity in m/sec
10	unit Reynolds number per cm

Table 1: Ludwieg tube flow parameters throughout run.

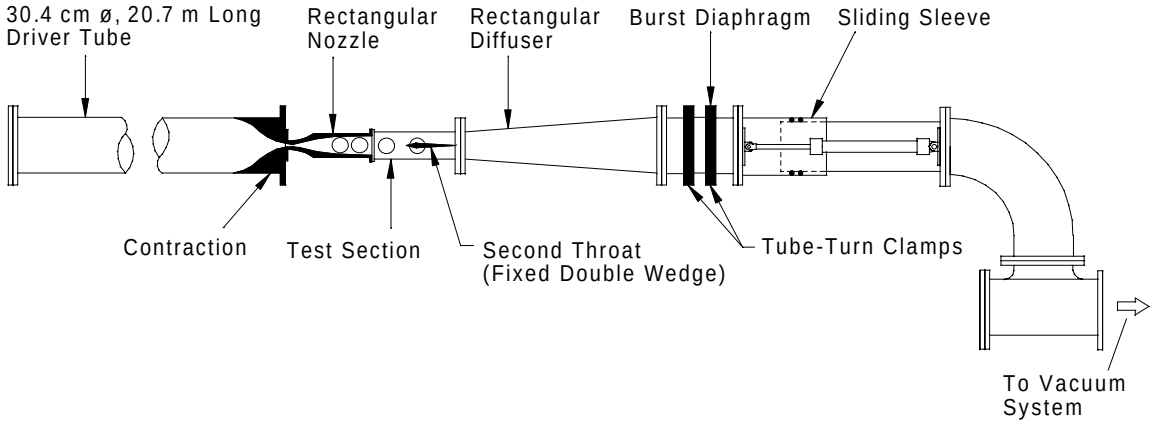

Figure 1: Sketch of Purdue quiet-flow Ludwieg tube.

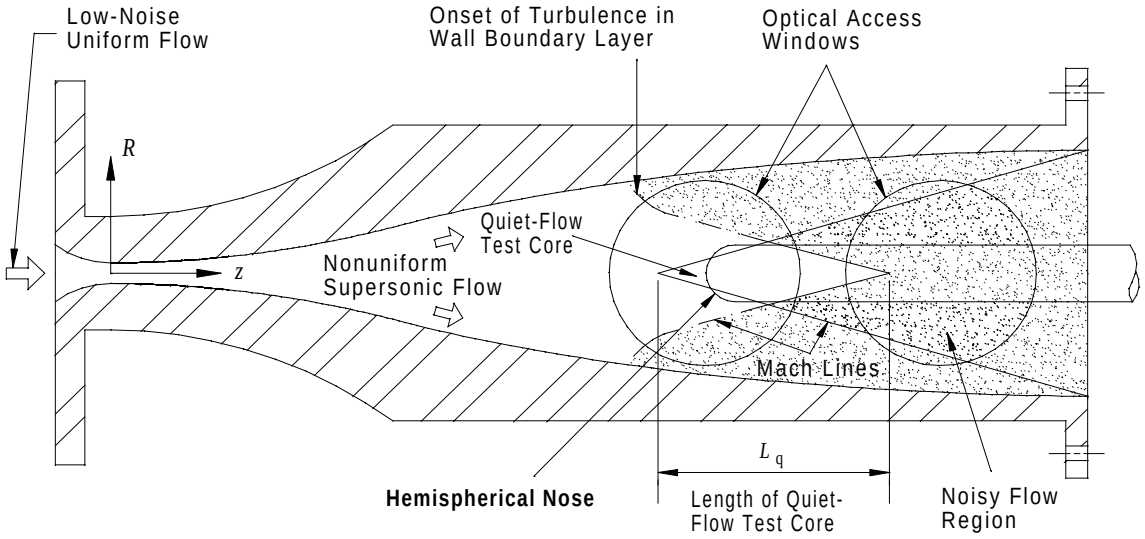

Figure 2: Blunt body in quiet-flow region of test section.

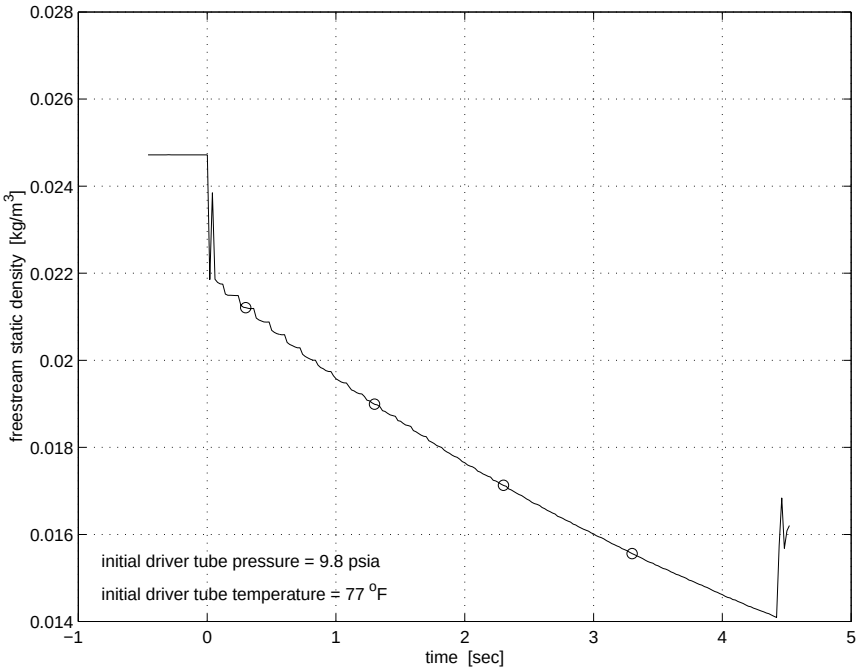

Figure 3: Static density drop throughout run.

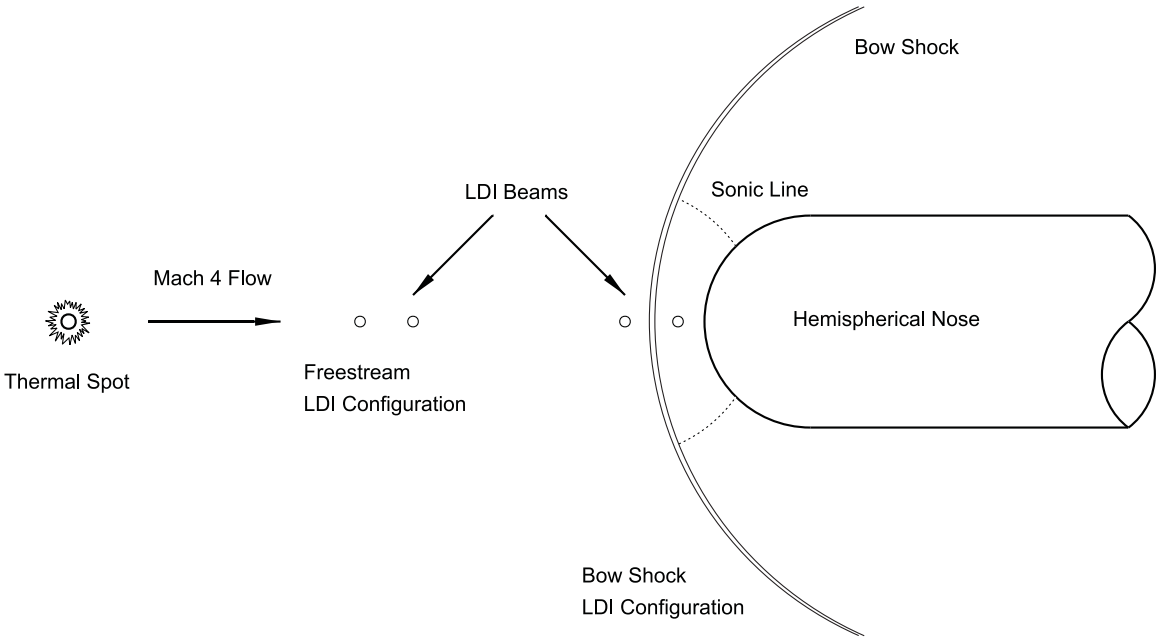

Figure 4: Test flow configuration with blunt body.

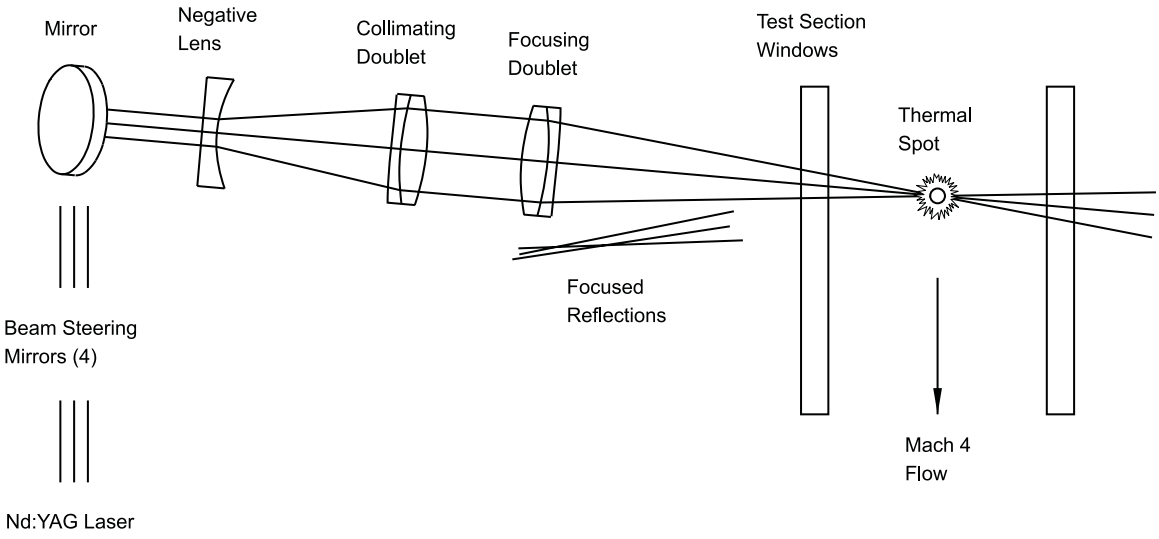

Figure 5: Schematic of thermal spot generation in Ludwieg tube.

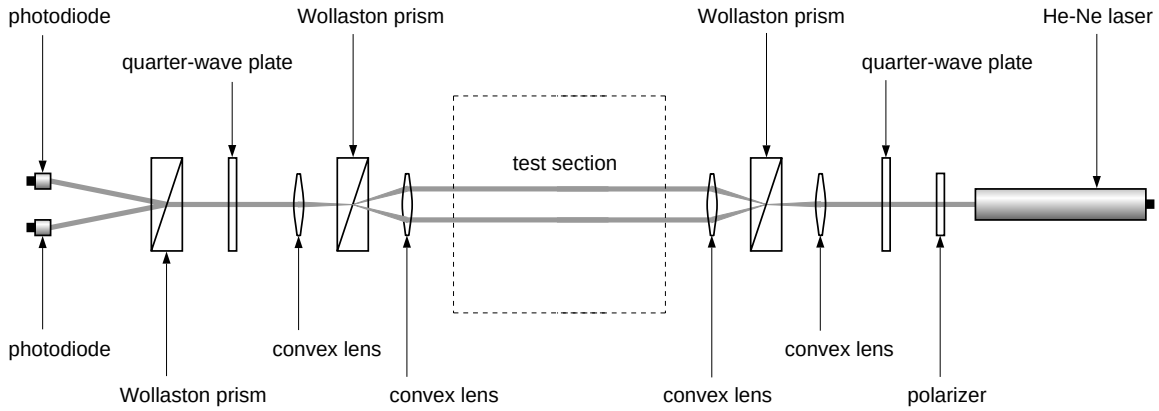

Figure 6: Schematic of basic laser differential interferometer.

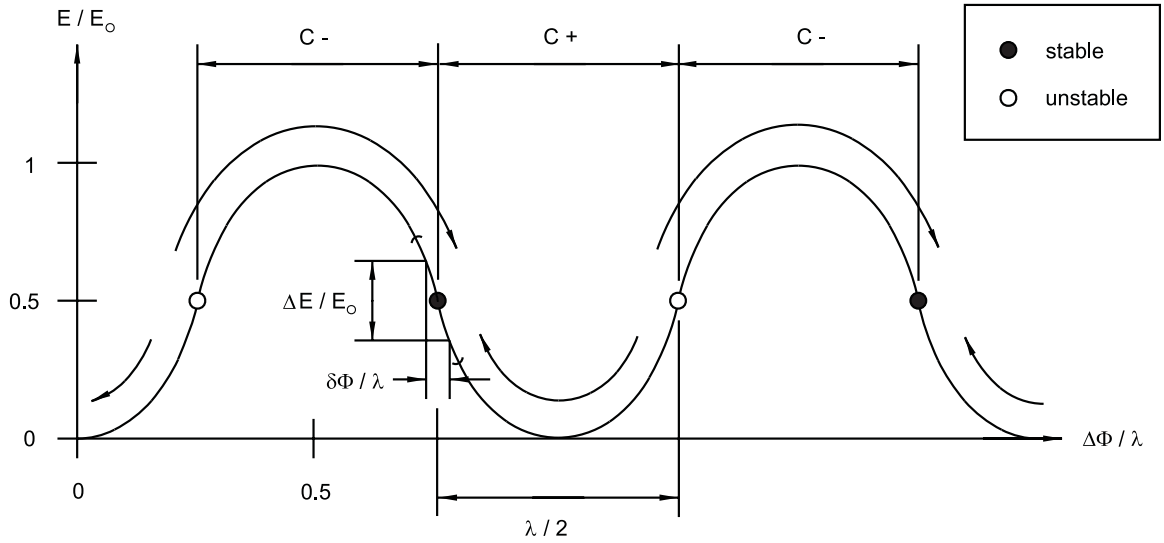

Figure 7: Laser differential interferometer interference slope.

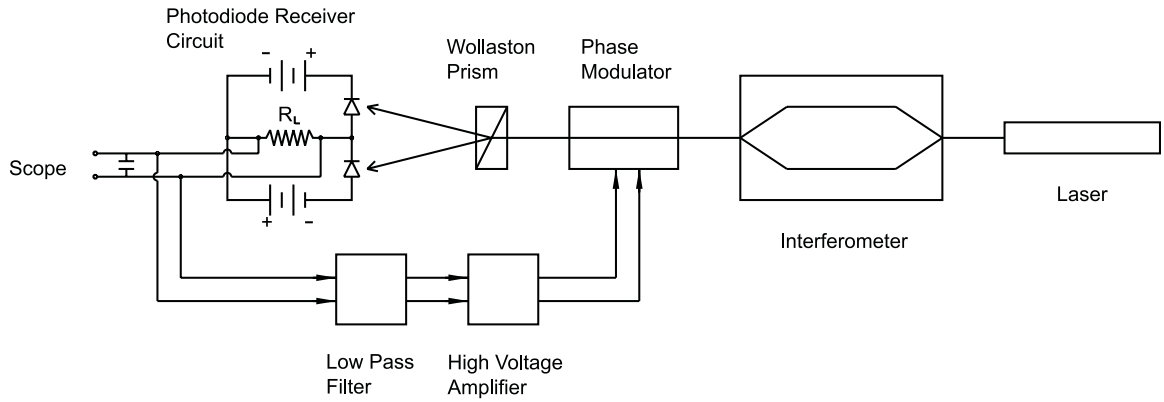

Figure 8: Photodiode analog differencing circuit with phase modulator feedback.

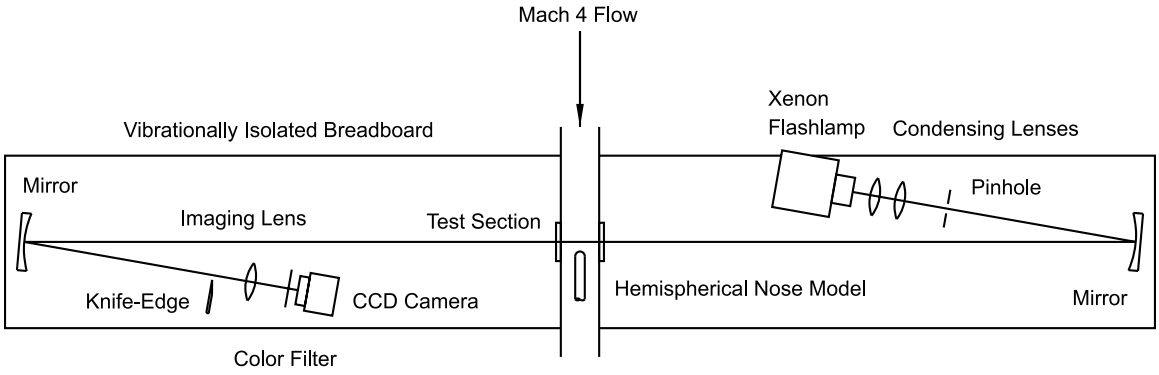

Figure 9: Schlieren system layout.

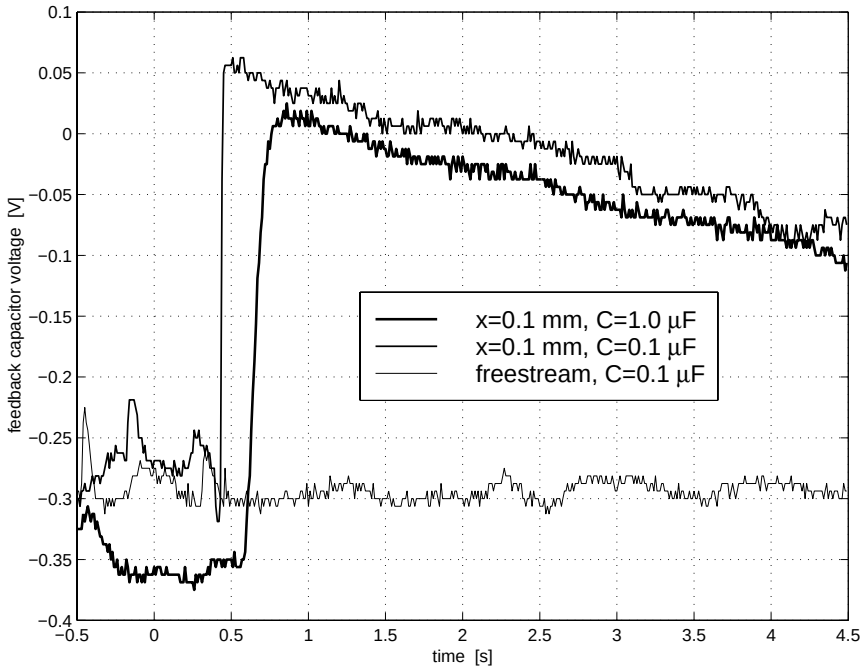

Figure 10: Voltage across feedback capacitor throughout run.

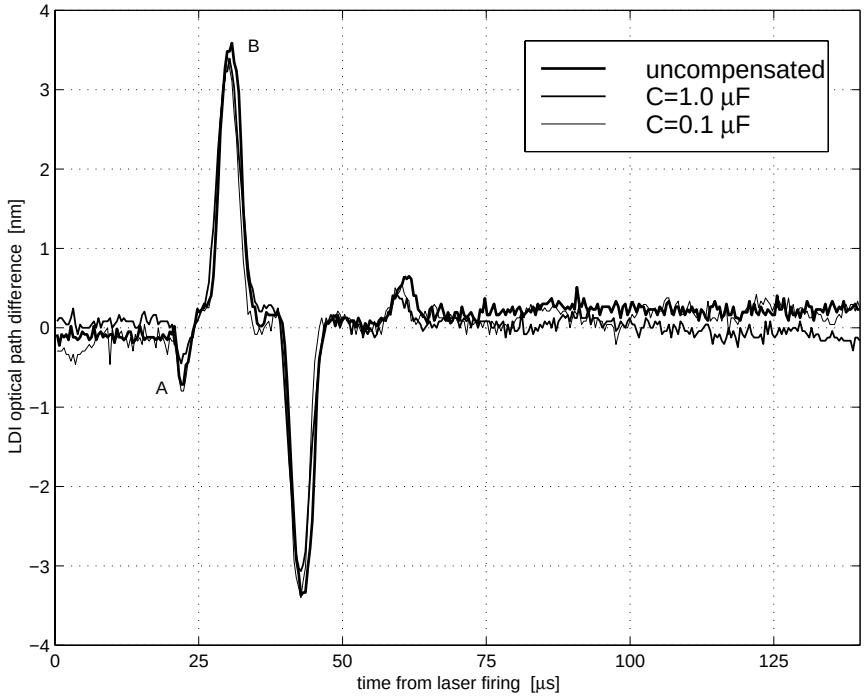

Figure 11: LDI response to thermal spot in freestream.

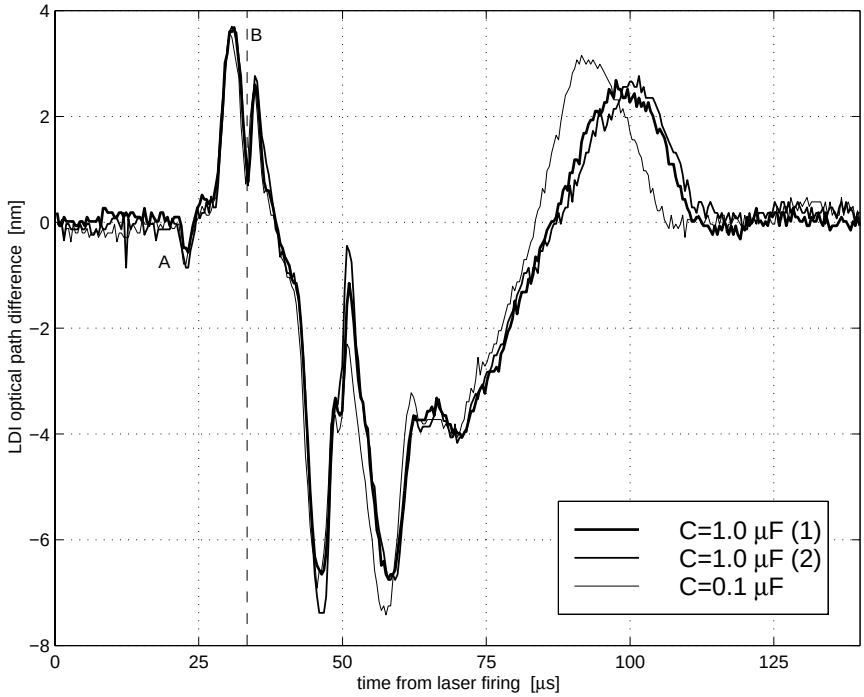

Figure 12: LDI response behind bow shock with thermal spot impinging.

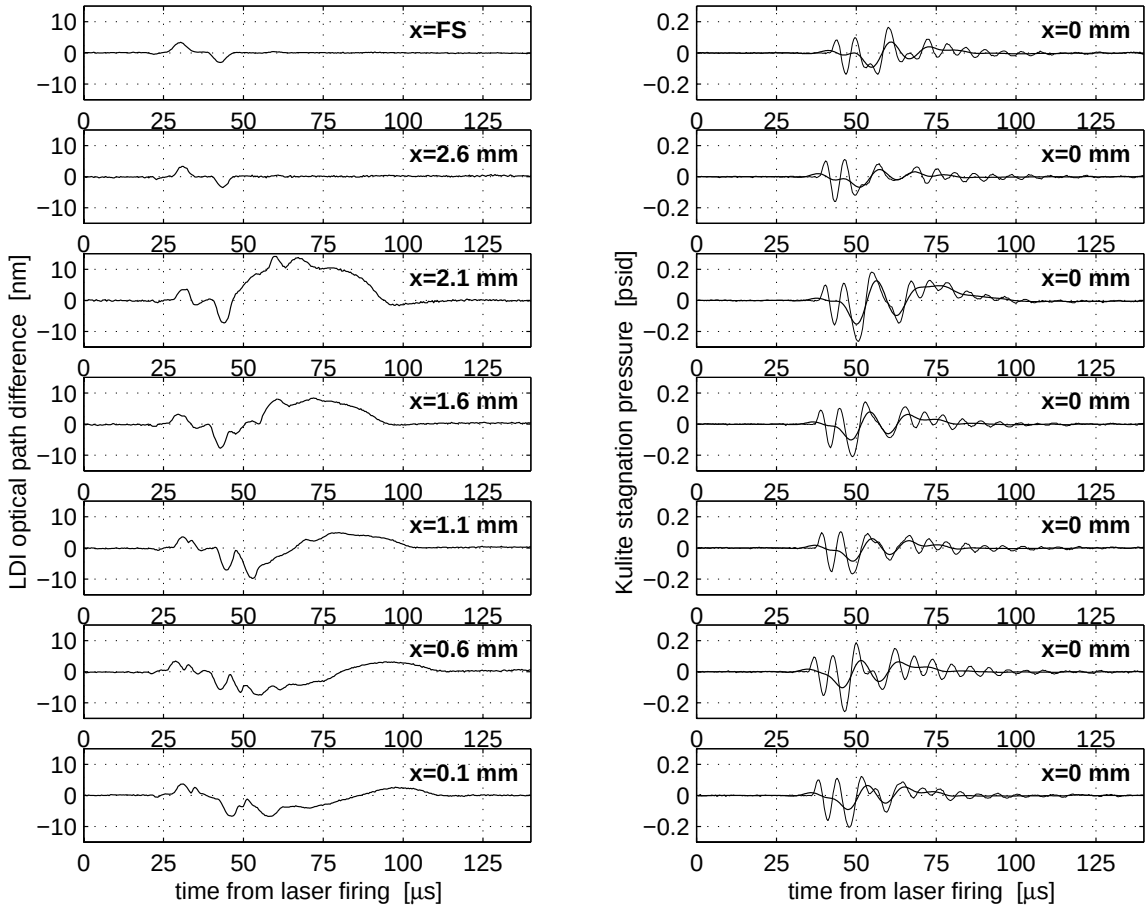

Figure 13: LDI and Kulite responses with thermal spot impinging on bow shock.

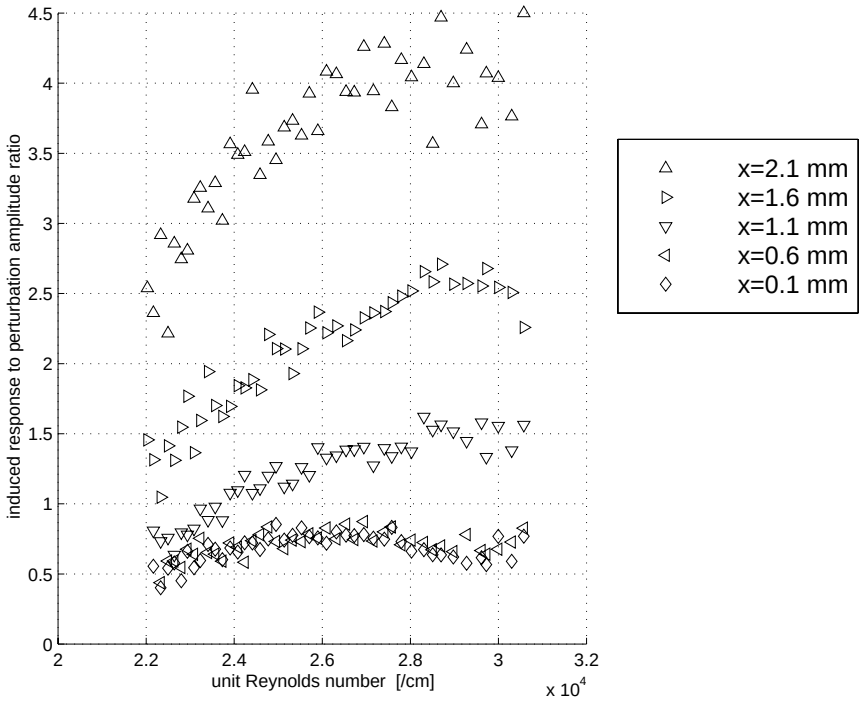

Figure 14: Induced response to perturbation amplitude ratios throughout run.

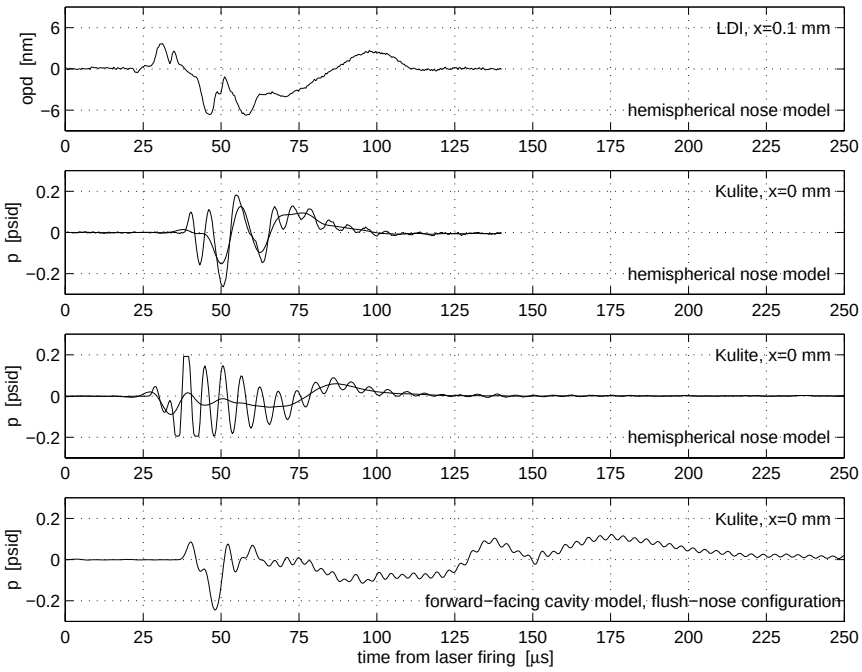

Figure 15: LDI and various Kulite responses to laser perturbation at nose of same and similar models.

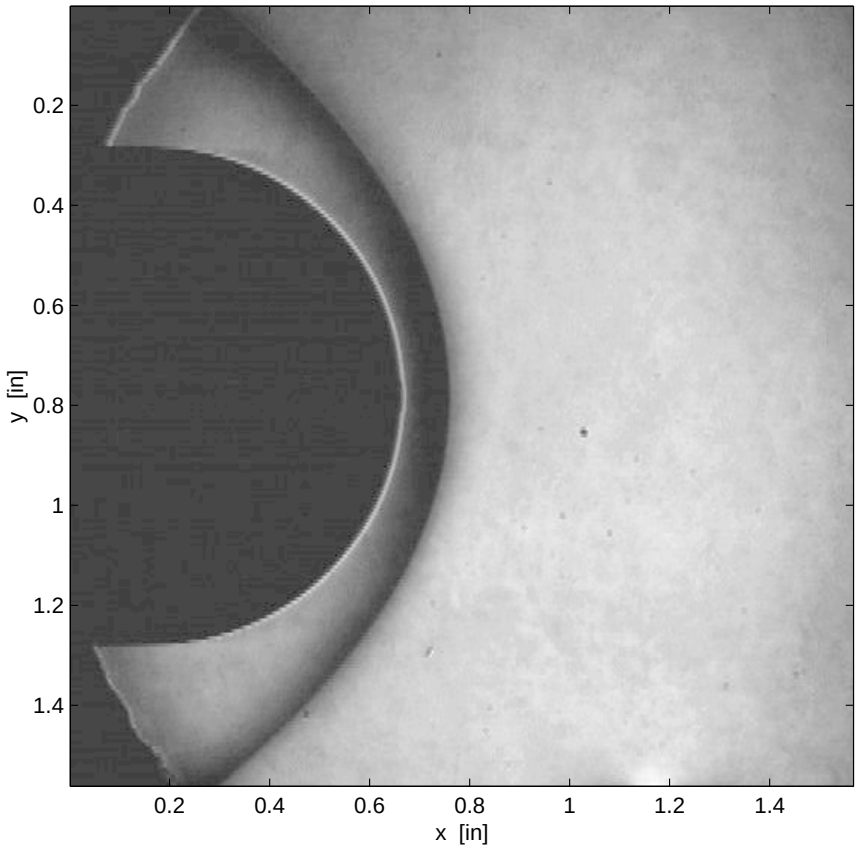

Figure 16: Schlieren image of Mach 4 flow over hemispherical nose model.

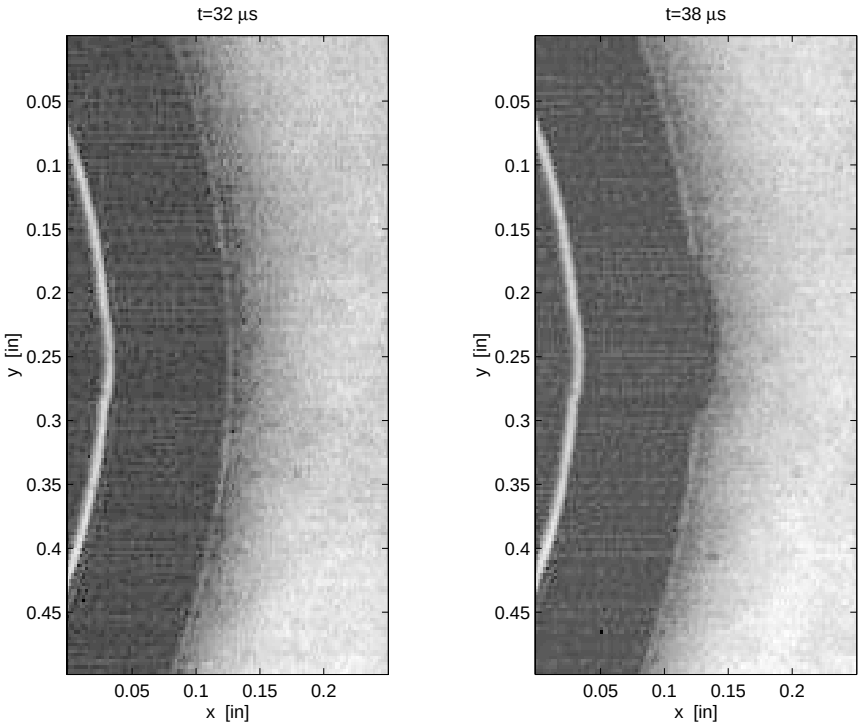

Figure 17: Schlieren images of thermal spot impinging on bow shock.

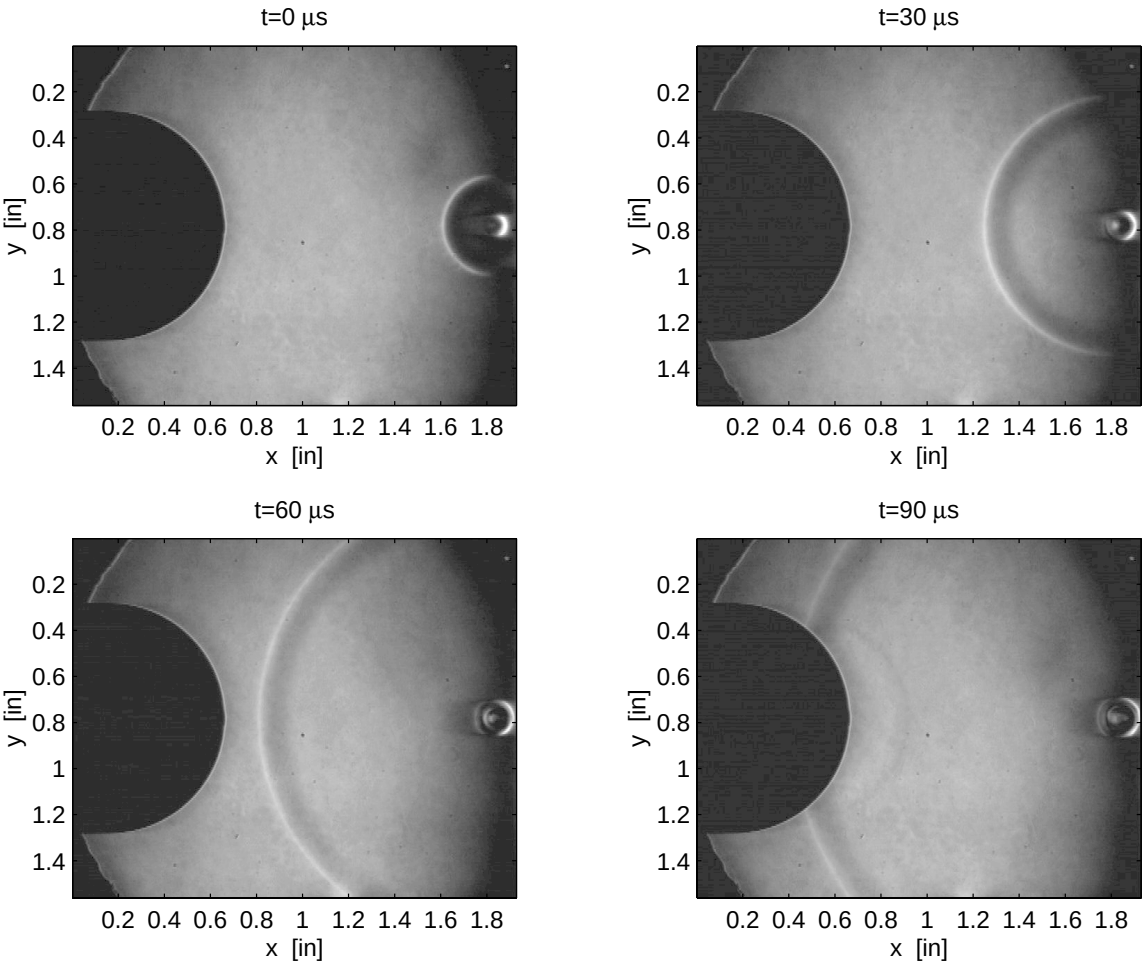

Figure 18: Schlieren images of thermal spot evolution. (no flow, atmospheric pressure)